Crystal Structure and Calculated Electronic Band Structure of ZrTe₃

Klaus Stöwe[1] and Frank R. Wagner

Institut für Anorganische Chemie und Analytische Chemie und Radiochemie, Universität des Saarlandes, 66041 Saarbrücken, Saarland, Germany

Because of inconsistencies in literature data, the crystal structure of ZrTe₃ was redetermined from single-crystal data and the electronic band structure was calculated using density functional theory in the local density approximation (LDA) and the linear muffin tin orbital method (LMTO). ZrTe₃ crystallizes in the monoclinic space group $P2_1/m$ with $a = 589.8(1)$ pm, $b = 392.69(3)$ pm, $c = 1010.3(1)$ pm, and $\beta = 97.81(1)°$ ($Z = 2$) in the ZrSe₃ structure type (ω data collection, $R_w = 1.88\%$). In the layer structure of ZrTe₃ almost linear homonuclear Te chains in [100] direction with alternating distances of 279.4(1) and 310.5(1) pm are observed. In addition to these, there are several other Te–Te distances below the sum of the radii of Te^{2-} ions (370–380 pm). From the band structure calculations we found these homonuclear contacts to be responsible for the unexpected metallic conductivity of ZrTe₃. The calculation of the Fermi surface revealed three branches. The one caused by the intersection of E_F with bands of predominantly Te chain character shows an extended region of approximately parallel Fermi surface. The nesting vector, which lies in the range $\vec{q} \approx (0.95 \pm 0.05)\vec{a}^* + (0.35 \pm 0.15)\vec{c}^*$, is in fair agreement with data from an electron diffraction study of ZrTe₃, which has shown the presence of a charge density wave at a temperature of 63 K with the vector $\vec{q} \approx 0.93\vec{a}^* + 0.33\vec{c}^*$. © 1998 Academic Press

INTRODUCTION

The crystal structure of ZrTe₃ was first published by Furuseth *et al.* (1) in 1975. They proposed that there are two different structural variants, named A and B, which both crystallize in the monoclinic space group $P2_1/m$. In variant B, which has been thought to be adopted by the compound ZrTe₃, the cation coordination polyhedron is much more distorted than in variant A, also known as the ZrSe₃ structure type, so that different interatomic distances are found in the two variants.

In the following decade, ZrTe₃ was the subject of numerous investigations because it was the only compound known beyond the trichalcogenides of this structure type which had metallic conductivity (2). Near 63 K the resistance exhibits a hump, which is associated with the formation of a charge density wave (CDW) (3). Single-crystal measurements (2, 4) reveal that this hump is observed only in the direction of the crystallographic $\vec{a}$- and $\vec{c}$-axes, but not along the chain direction of the zirconium ions, i.e., the $\vec{b}$-axis. An extended-Hueckel (EH) electronic band structure study of the resistivity hump in ZrTe₃ was published by Canadell *et al.* (5). Below 2 K ZrTe₃ becomes superconductive, whereby superconducting filaments appear with a pacing of 4 nm parallel to the $\vec{a}$-axis in a nonsuperconducting matrix (3). The nature of the filaments is not known. Both the metallic conductivity and the superconducting properties were associated (6) with linear chains of equidistant Zr^{4+} ions in the [010] direction, because this type of chain is also found in the metallic compound NbSe₃, where the Nb coordination topology is quite similar. There the linear Nb^{4+} chains are considered to be the dominant factors for the charge density wave formation at temperatures of 145 and 59 K (7). Experimental evidence for this thesis stems from electron diffraction investigations (7), where (incommensurate) superlattice reflections in the direction of the Nb chains can be observed below the transition temperature.

In 1991, chronologically after all the aforementioned investigations and calculations, the crystal structure of ZrTe₃ was redetermined by Furuseth *et al.* (8). In the course of this investigation, no indications for the structural variant B were found and it was ascertained that ZrTe₃ crystallizes exclusively in variant A. The former error was explained by the fact that "… the earlier studies were hampered by twinning effects, impurities or by other unforeseen factors …" (8). From the EH band structure calculations of Canadell *et al.* (5) for ZrTe₃ crystallizing in variant A, semiconducting properties are deduced, whereas variant B should be metallic. Because of this inconsistency, we felt obliged to redetermine the crystal structure and electronic band structure of ZrTe₃.

EXPERIMENTAL

Sample Synthesis

Black platelike single crystals of ZrTe₃ up to an edge length of several millimeters were obtained by chemical

---

[1]To whom correspondence should be addressed.

vapor transport reactions in silica ampules with I_2 or $TeBr_4$ as transporting agent in a temperature gradient from 700 to 600°C starting from the elements Zr (foil, 99.9 + %, Heraeus, Karlsruhe, Germany) and Te (pieces, >99.999%, Fluka, Buchs, Switzerland) as reported earlier (8).

X-Ray Single-Crystal Structure Determination

The data collections were carried out with a P4 single-crystal diffractometer (Siemens, Karlsruhe, Germany), and the structure solution and refinement were performed with the computer program SHELXTL (9). Tables 1–3 give a summary of important measurement and refinement data, including the refined parameters, and Table 4 gives selected interatomic distances below 500 pm.

TABLE 1
Measurement and Refinement Data for ZrTe₃ in the X-Ray Single-Crystal Structure Analysis

Measurement temperature	293 K
Lattice parameters	
a	589.8(1) pm
b	392.69(3) pm
c	1010.3(1) pm
β	97.81(1)°
Number of formula units per cell	2
Calculated density	6.790 g cm^{-3}
Space group	$P12_1/m1$
Measured range of reciprocal space (MoKα)	$3 < 2\theta < 60°$ (all octants)
Type of data collection/scan width	$\omega/0.8°$ in 96 steps
Number of observed reflections	2672
Number of nonequivalent reflections	762
Absorption correction	Numerical[a,b]
Crystal color	Lustrous black
Crystal size	$0.18 \times 0.30 \times 0.06$ mm^3
Linear absorption coefficient	207.03 cm^{-1}
Internal R value[c]	2.31%
Program for structure solution and refinement	SHELXTL PLUS[d]
Structure solution by	Direct methods
Structure refinement by	Full-matrix least squares
Number of independent parameters	26
Extinction parameter χ (empirical, with $F^* = F[1 + 0.002\chi F^2/\sin(2\theta)]^{-1/4}$	0.0242(3)
R values ($w = 1/\sigma(F_o)^2$)	$R = 2.33\%$, $R_w = 1.88\%$

[a]W. Herrendorf, HABITUS, Program for the Optimization of the Crystal Description for a Numerical Absorption Correction on the Basis of Appropriate Psi-Scanned Reflections, Karlsruhe, Germany, 1992.

[b]N. W. Alcock, P. J. Marks, and K.-G, Adams, ABSPSI, Absorption Correction and Refinement of the Crystal Habitus, Karlsruhe, Germany, 1994.

[c]K.-G. Adams, MITTELN, Averaging Symmetry-Equivalent Reflections, Karlsruhe, Germany, 1995.

[d]SHELXTL PLUS, version 4.0, Program for Determination of Crystal Structures with X-Ray and Neutron Data, Siemans Analytical X-Ray Instruments, Inc., Madison, WI, 1990.

TABLE 2
Positional Parameters and Equivalent Isotropic Displacement Factors (pm²) of ZrTe₃

Atom	Wyckoff position	x	y	z	U_{eq}[a]
Zr	2e	0.28836(8)	0.25	0.66574(6)	129(1)
Te (1)	2e	0.76359(5)	0.25	0.55524(4)	133(1)
Te (2)	2e	0.43267(6)	0.25	0.16744(4)	183(2)
Te (3)	2e	0.90479(6)	0.25	0.16093(4)	190(2)

[a]Equivalent isotropic U calculated by $\frac{1}{3}[U_{22} + (U_{11} + U_{33} + 2U_{13}\cos\beta)/\sin^2\beta]$.

CRYSTAL STRUCTURE

The structural data of our own investigations are in accordance with those of the reexamination published previously by Furuseth *et al.* (8). They improve ($R_w = 1.9\%$, reduced esd's) the data of the former investigation ($R_w = 5.9\%$). As for the other zirconium trichalcogenides ZrQ_3 (Q = S, Se), the values relate to the structural variant A, i.e., the $ZrSe_3$ structure type. Each zirconium ion is surrounded in this structure type by eight anions forming a twofold capped trigonal prism as coordination polyhedron, which is shown in Fig. 1. Sharing common trigonal faces, the prisms are stacked to infinite rods in the [010] direction. Due to this arrangement, chains of equidistant Zr^{4+} ions with the periodicity of the $\vec{b}$ translation are observed. In the [100] direction the prism rods are packed in such a way that the Te(1) ions of one rod serve as prism caps of the neighboring rod. Within these prism slabs almost linear chains of Te(2) and Te(3) ions ($\angle$Te–Te–Te = 177.5(5)°) with alternating distances of 279 and 310 pm are found. The shorter one, d_1, within one prism (see Table 4 and Fig. 1) is comparable to a single covalent bond length [271 pm in diphenylditelluride (10)]. The longer one, d_2, from prism to prism is significantly shorter than in the isotypic semiconducting compound UTe_3, where the analogous Te(2)–Te(3) distances are $d_1 = 275$ pm and

TABLE 3
Anisotropic Displacement Factors (pm²) of ZrTe₃[a]

Atom	U_{11}	U_{22}	U_{33}	U_{23}	U_{13}	U_{12}
Zr	112(2)	106(3)	93(3)	0	15(2)	0
Te(1)	115(2)	126(2)	86(2)	0	14(1)	0
Te(2)	114(2)	149(2)	140(2)	0	3(1)	0
Te(3)	135(2)	154(2)	149(2)	0	52(2)	0

[a]The dimensions are in accordance with the formula

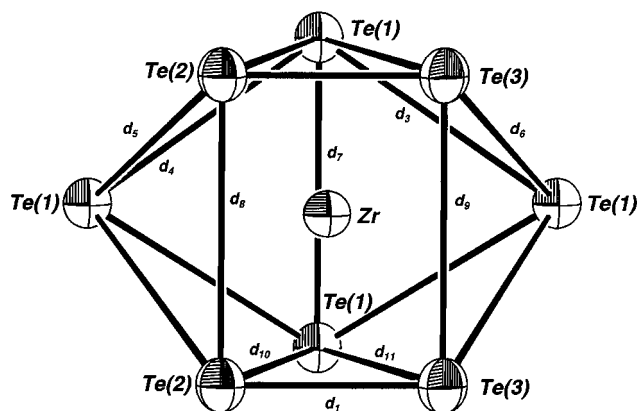$$-2\pi^2 \sum_i \sum_j U_{ij}h_i h_j a_i^* a_j^*.$$

FIG. 1. Coordination polyhedron of the Zr ions in $ZrTe_3$ (ORTEP plot with 95% probability ellipsoids).

TABLE 4
Selected Interatomic Distances below 500 pm in $ZrTe_3$ (pm)

Zr–Te distances			Te–Te distances		
Zr–Te(2)	294.1(1)	2×	Te(2)–Te(3)	279.4(1)	d_1
Zr–Te(1)	295.8(1)	2×	Te(2)–Te(3)	310.5(1)	d_2
Zr–Te(3)	296.0(1)	2×	Te(1)–Te(1)	370.4(1)	d_3
Zr–Te(1)	314.4(1)	1×	Te(1)–Te(1)	371.8(1)	d_4
Zr–Te(1)	315.5(1)	1×	Te(1)–Te(2)	373.2(1)	d_5
			Te(1)–Te(3)	379.2(1)	d_6
Zr–Zr distances			Te(1)–Te(1)	392.7(1)	d_7
Zr–Zr	392.7(1)		Te(2)–Te(2)	392.7(1)	d_8
Zr–Zr	485.3(1)		Te(3)–Te(3)	392.7(1)	d_9
Zr–Zr	485.5(1)		Te(1)–Te(2)	413.3(1)	d_{10}
			Te(1)–Te(3)	417.9(1)	d_{11}

$d_2 = 335$ pm, respectively (11). These tellurium chains in $ZrTe_3$ have remained undiscussed in the literature till today, but, as we will show in the next sections, they are crucial to the understanding of the metallic behavior of the compound. In addition to these homonuclear tellurium distances, several others shorter than the sum of the radii of Te^{2-} ions are found in $ZrTe_3$. Specifically, these are the distances of the prism caps to the prism ions (d_3–d_6; see Fig. 1 and Table 4) and between the trigonal prism faces (d_7–d_9). Finally, in the [001] direction the noncapped prism faces are staggered face to face in a layer-type structure. This arrangement of polyhedra is depicted in Fig. 2. The Te–Te interchain distances across the van der Waals gap are larger than 400 pm, a value which gives a clue for the upper distance limit for relevant homonuclear tellurium bonds.

DETAILS OF THE ELECTRONIC BAND STRUCTURE CALCULATIONS

LDA LMTO-ASA Calculations

The electronic structure calculations were performed by use of density functional theory in the local density approxi-

mation (LDA) with the LMTO-47 package of Andersen *et al.* (12). The calculation within the atomic spheres approximation (ASA) includes corrections for the neglect of the interstitial region and the partial waves of higher order (ASA + combined correction). To reduce as much as possible the overlap between the atomic spheres, empty interstitial spheres were added to the potential. The construction of the ASA radii was done by an automatic procedure of the program package using the method proposed by Andersen (13). In detail, the sphere radii (in pm) are as follows:

Zr	Te(1)	Te(2)	Te(3)	E1(2e)	E2(2e)
173.3	169.3	161.7	161.7	138.3	124.0
E3(2e)	E4(2e)	E5(2e)	E6(4f)	E7(2e)	E8(2e)
106.4	104.7	82.5	74.9	76.2	75.3

The basis set consisted of the Zr 5s, 5p, and 4d, the Te 5s and 5p, and the interstitial 1s LMTOs. The Zr 4f, the Te 5d and 4f, and the interstitial p and d partial waves were included only in the tails of these LMTOs according to the Löwdin down-folding procedure (13).

Brillouin Zone

The reciprocal lattice vectors together with the first Brillouin zone are shown in Fig. 3. As the deviation of the
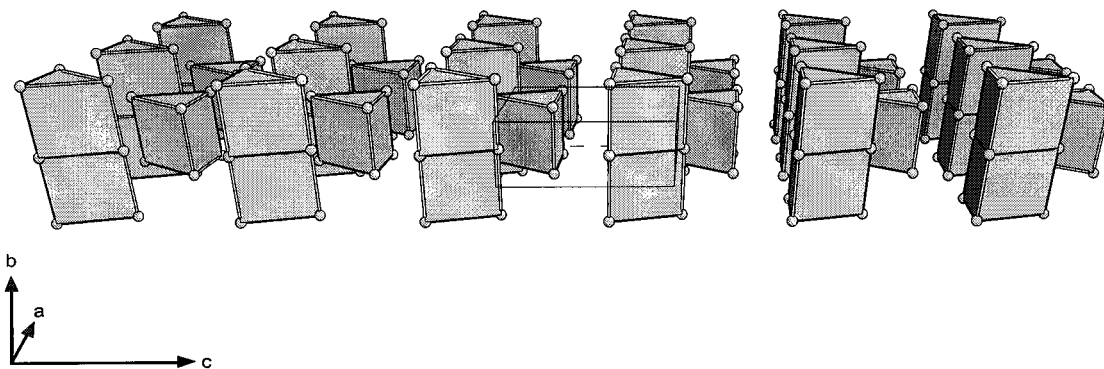

FIG. 2. Crystal structure of $ZrTe_3$ in a [100] projection (tilted by $\approx 30°$). For simplification, line drawings from the prisms to the caps are omitted.
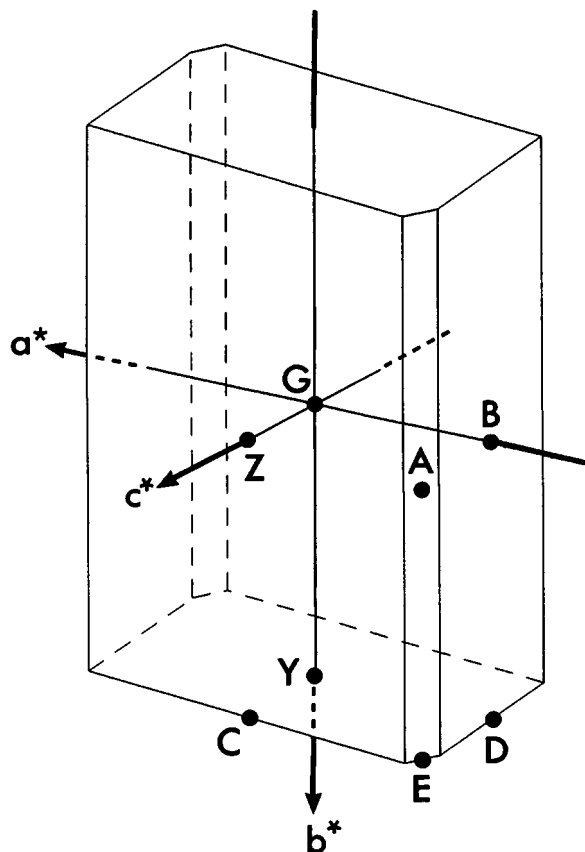
FIG. 3. Brillouin zone and high-symmetry points in ZrTe₃.

FIG. 4. Band structure of ZrTe₃.

monoclinic angle from 90° is relatively small, the Brillouin zone has the shape of a rhombus with two small additional facets where the rhombus faces meet at an acute angle (with a monoclinic angle of 120°, the Brillouin zone would have the form of a regular hexagonal prism). High-symmetry points were labeled following Miller and Love (14).

RESULTS OF THE ENERGY BAND AND FERMI SURFACE CALCULATIONS FOR ZrTe₃

LDA LMTO-ASA Calculations

The calculated energy band structure of ZrTe₃ is shown in Fig. 4 for the wave vector $\vec{k}$ along the following lines (see Fig. 3): $G = (0, 0, 0)$ to $Z = (0, 0, \frac{1}{2})$ to $C = (0, \frac{1}{2}, \frac{1}{2})$ to $Y = (0, \frac{1}{2}, 0)$ to $E = (-\frac{1}{2}, \frac{1}{2}, \frac{1}{2})$ to $A = (-\frac{1}{2}, 0, \frac{1}{2})$ and back to $G = (0, 0, 0)$ and then to $B = (-\frac{1}{2}, 0, 0)$ to $D = (-\frac{1}{2}, \frac{1}{2}, 0)$ to $Y = (0, \frac{1}{2}, 0)$ and again back to $G = (0, 0, 0)$. The coordinates are given in units of the reciprocal lattice vectors. The band structure was projected onto the following orthogonal LMTOs normalized to unity within the ASA spheres: the $5p_x$, $5p_y$, and $5p_z$ orbitals of the two different kinds of tellurium ions, the isolated ones (Te(1)) and the ones within the homonuclear chains (Te(2) and Te(3)), as well as the
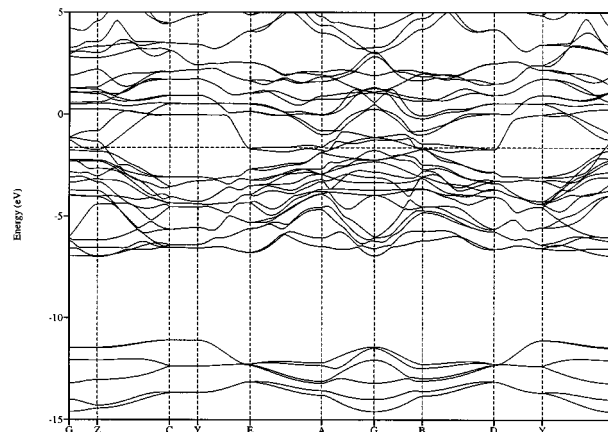
entire $4d$ orbitals and separately the $4d_{y^2}$ orbital of Zr. In such a "fat" band structure (examples are given in Figs. 5a–c) each band is given a width which is proportional to the weight or the sum of the weights of the corresponding orbital or orbitals. In Fig. 5 an orbital character of 100% is equivalent to $\frac{1}{20}$ of the total energy scale. For a scale of -7.5 to 2.5 eV, this is 0.5 eV.

A semiconducting MQ_3 compound of this structure type, e.g., ZrS₃, can be formulated in its ionic extreme as $M^{4+}Q^{2-}(Q_2)^{2-}$ with Q_2 dumbbells according to the Zintl–Klemm–Busmann concept (15). Thus with two formula units per cell, we would expect 6 $Q(ns)$ and $16Q(np)$ bands to lie below the Fermi level. Two of these filled p-bands with mainly Q contributions are Q–Q σ bands, whereas two other Q–Q $pp\sigma^*$ bands should lie above E_F. In ZrTe₃ the 6 Te(5s) bands are found in the range from -15 to -11 eV[2] and 16 bands with predominantly Te(5p) character lie in the range from -7 to -1 eV, as we can see from Fig. 4. However, contrary to a semiconducting compound, in metallic ZrTe₃ some of these bands are intersected by the Fermi level at -1.6 eV. Above -2 eV, we find the Zr(4d) bands as well as the remaining two Te(5p) bands. The Zr(5s) states lie above 2 eV and are irrelevant for the bonding in ZrTe₃. Due to the fact that there are two symmetry-equivalent ZrTe$_{6/2}$ trigonal prisms in the unit cell, the bands in Fig. 4 run in a pairwise manner, with relatively small differences in each pair along directions in reciprocal space, where degeneracy is removed by symmetry.

From Fig. 5c we see that the two Te(5p)$pp\sigma^*$ bands above -2 eV are Te(2)/Te(3) (5p$_x$) bands. In the [100] direction the linear homonuclear Te chains are running with alternating distances (vide supra). At $G = (0, 0, 0)$ the energy difference between the $p_x p_x \sigma$ bands below E_F and the $p_x p_x \sigma^*$

[2]The absolute values of the band energies are not related to ionization energies via Koopman's theorem. Their explicit use in the discussion serves only for orientation.
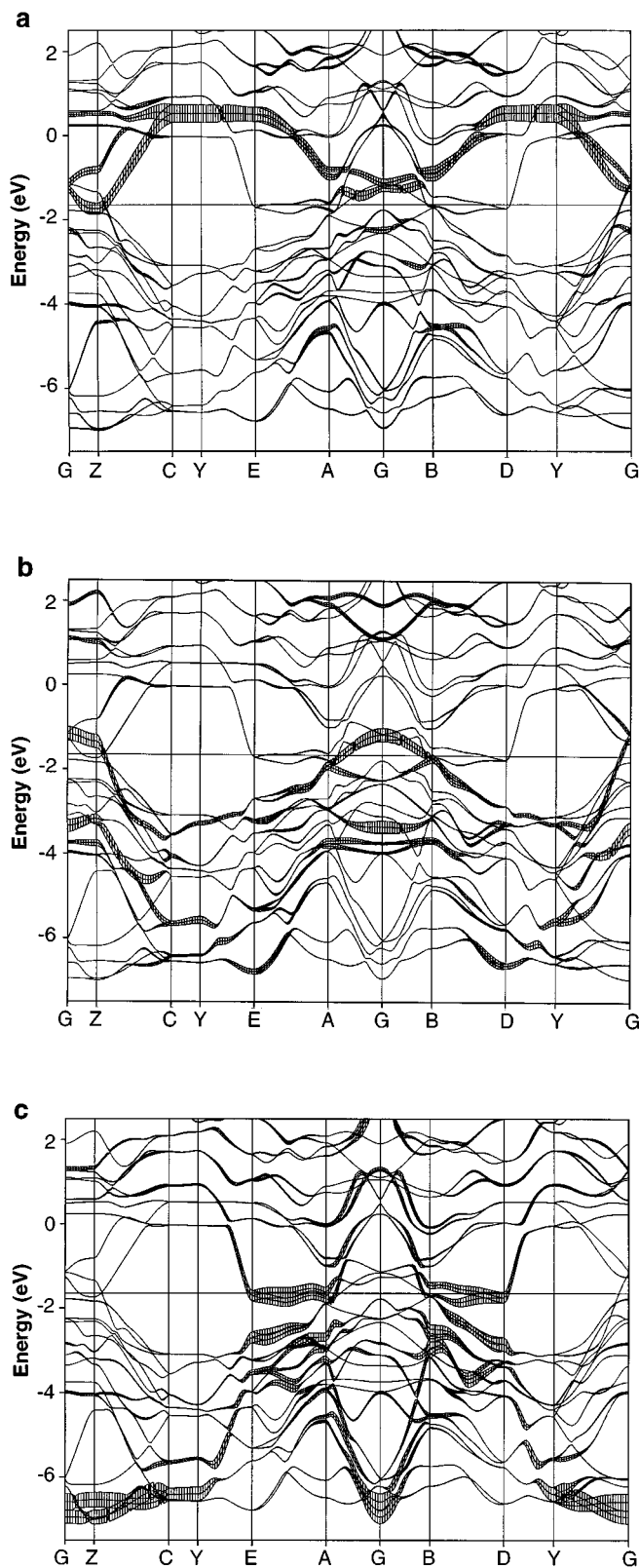
FIG. 5. Energy bands of $ZrTe_3$ decorated with orthonormal-orbital characters. A pure band state is given the energy width 0.5 eV: (a) $Zr(4d_{y^2})$ "fat" band; (b) $Te(1)(5p_y)$ "fat" band; (c) $Te(2)/Te(3)(5p_x)$ "fat" band.

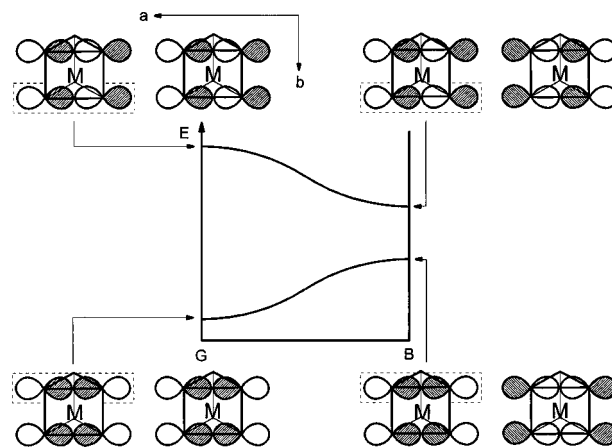**FIG. 6.** Dispersion of the $Te(2)/Te(3)$ $(5p_x)$ bands along the line $G = (0, 0, 0)$ to $B = (-\frac{1}{2}, 0, 0)$.

bands is largest. It decreases along the line G to $B = (-\frac{1}{2}, 0, 0)$. This is shown schematically in Fig. 6 for compounds with $ZrSe_3$ structure type in general. The larger the alternation in the linear chain, the larger is the gap at point B. In compounds such as ZrS_3, $ZrSe_3$, or UTe_3, the Fermi energy is found within the gap, so these compounds are semiconductors. In the compound $ZrTe_3$, along the lines $B = (-\frac{1}{2}, 0, 0)$ to $D = (-\frac{1}{2}, \frac{1}{2}, 0)$ and $A = (-\frac{1}{2}, 0, \frac{1}{2})$ to $E = (-\frac{1}{2}, \frac{1}{2}, \frac{1}{2})$ the $5p_x$ bands of $Te(2)$ and $Te(3)$ are so low in energy that they intersect E_F. As a consequence, additional antibonding states in the shorter $Te(2)$–$Te(3)$ bond d_1 and additional bonding states in the longer $Te(2)$–$Te(3)$ bond d_2 are occupied in $ZrTe_3$ compared to, for example, ZrS_3 or UTe_3. This can also be seen in the two bond lengths if compared with those in the semiconducting compound UTe_3 (279 and 310 pm in $ZrTe_3$ compared to 275 and 335 pm in UTe_3). Along the lines B to D and A to E the $Te(2)/Te(3)$ $(5p_x)$ bands exhibit only weak dispersion with saddle points in the energy versus momentum relation. This constellation is similar to a van Hove singularity (16). As a consequence, a high density of states at the Fermi level occurs. The appearance of extended van Hove singularities, as found in ceramic superconductors such as $Bi_2Sr_2CaCuO_8$, is responsible for the high transition temperatures of these compounds (17).

However, only the E_F intersection of the $Te(2)/Te(3)(5p_x)$ bands is not the sole reason for metallic conductivity in $ZrTe_3$; several other bands are also intersected. In detail, these are the $Te(1)(5p_y)$ and $Zr(4d_{y^2})$ bands. In $ZrTe_3$, apart from the two short homonuclear $Te(2)$–$Te(3)$ distances in the linear chain, there are several other Te–Te distances below the sum of the radii of Te^{2-} ions (d_3–d_9; see discussion of the crystal structure). Near E_F the interaction of the $Te(1)(5p_y)$–$Te(1)(5p_y)$ orbitals along lines with large $\vec{a}^*$ and $\vec{b}^*$ components becomes noticeable. Both are directions

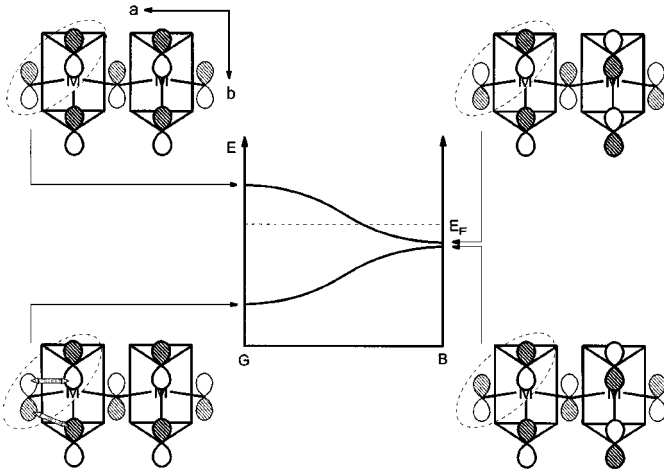**FIG. 7.** Dispersion of the Te(1)($5p_y$) orbitals in ZrTe₃ along the line $G = (0, 0, 0)$ to $B = (-\frac{1}{2}, 0, 0)$.

in which the Te(1)–Te(1) distances d_3 and d_4 have large components in real space. This is depicted in Fig. 7 exemplarily for the dispersion along the line $G = (0, 0, 0)$ to $B = (-\frac{1}{2}, 0, 0)$. For simplification, the Bloch orbitals of Te(2) and Te(3) are omitted. The mixing with orbitals of Te(2) and Te(3) is significant since the distances of Te(1) to Te(2) and Te(3) are not much longer than to other Te(1). The energy of the two Te(1)($5p_y$) bands at point B is not exactly the same since the two distances d_3 and d_4 are slightly different (see Table 4). The weak interaction of the trigonal prism rods with each other, mentioned earlier, is strong enough to destabilize one of the Te(1)($5p_y$) bands above the $pp\sigma^*$ states of the other tellurium ions. According to this destabilization, Te(1)($5p$) states are depleted, so that the notation of ZrTe₃ within the Zintl–Klemm–Busmann concept, as given earlier, is actually not precise.

Due to the in-phase combination of the Zr($4d_{x^2-z^2}$) and Zr($4d_{xz}$) with the Te(1)($5p_x$) and ($5p_z$) Bloch functions, the former are removed from the region of the Zr($4d_{y^2}$) functions and raised in energy up to the top edge of the $4d$ band region (beyond the bands shown in Fig. 4). Therefore the $4d_{y^2}$ bands are energetically the lowest of all $4d$ states and reveal a dispersion only in the chain direction of the metal ions, e.g., $Z = (0, 0, \frac{1}{2})$ to $C = (0, \frac{1}{2}, \frac{1}{2})$ or $B = (-\frac{1}{2}, 0, 0)$ to $D = (-\frac{1}{2}, \frac{1}{2}, 0)$. In compounds such as NbS₃, which crystallizes in a structure closely related to the ZrSe₃ type[3] (18), or NbSe₃, with a very similar structure topology (also with trigonal prism chains; vide supra) (7), the $4d_{y^2}$ bands are half-filled and lead to the typical Peierls-type distortion and CDW phenomena. In ZrTe₃ these bands lie above the Fermi level, with the only exception along the line $G = (0, 0, 0)$ to $Z = (0, 0, \frac{1}{2})$, where

[3] NbS₃ crystallizes at ambient temperature in a distorted ZrSe₃ type with Nb₂ pairs.

one Zr($4d_{y^2}$) band is lowered below E_F. This effect is mainly due to the fact that the loss of the out-of-phase combination of Zr($4d_{y^2}$) and Te(1)($5p_z$) orbitals decreases the crystal orbital energy of the lower lying band from G to Z (see Fig. 8). On the other hand, the crystal orbital energy of the upper band is shifted by about 0.3 eV by an interlayer interaction.

The band structure calculation presented above has shown that the metallic conductivity of ZrTe₃ is not necessarily coupled with the existence of the structural variant B as stated in ref 5. For variant A, in which ZrTe₃ crystallizes in fact, metallic behavior is to be expected, too. The metallic conductivity seems to be caused essentially by the homonuclear Te chains in the [100] direction. This thesis is further illustrated by the Fermi surface plots.

Fermi Surface Calculation

In Fig. 9 the cross section of the calculated Fermi surface with $k_z = 0$ is shown. ZrTe₃ reveals a Fermi surface with three branches: around point $G = (0, 0, 0)$ the cross section of E_F (symbolized by small circles) includes a hole pocket region in which 15 valence bands (without Te($5s$)) are occupied. From Fig. 5b we can gather that the intersected band has predominantly Te(1)($5p_y$) character. The second branch of the cross section consists of only slightly curved, i.e.,
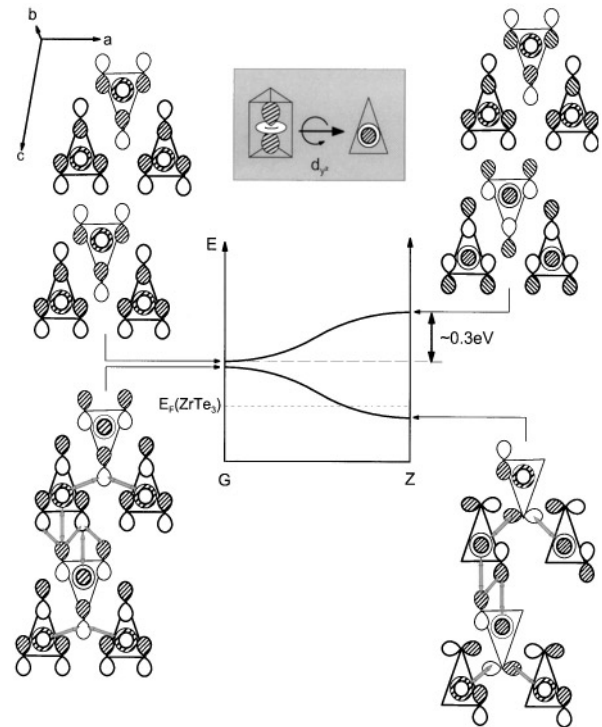

FIG. 8. Dispersion of the Zr($4d_{y^2}$) bands along the line $G = (0, 0, 0)$ to $(Z = 0, 0, \frac{1}{2})$. Remember that there are two trigonal-prismatic units within a unit cell. The interlayer interaction shifts the crystal orbital energies of the upper band by about 0.3 eV.
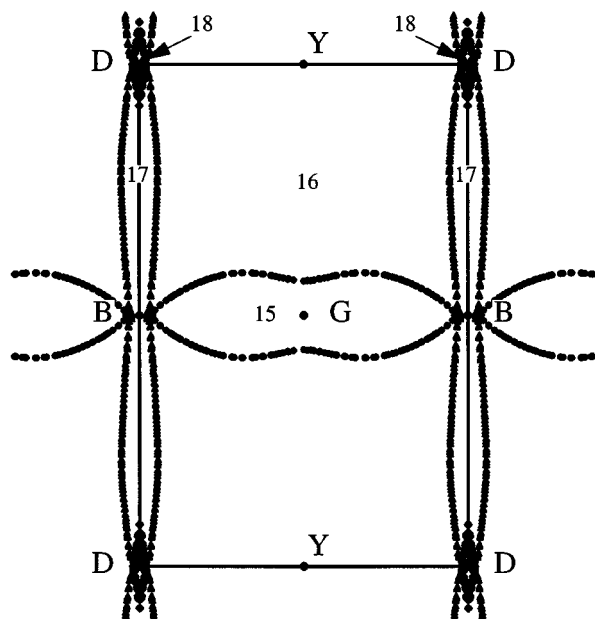
FIG. 9. Intersection of the Fermi surface and Brillouin zone of ZrTe$_3$ with the $k_z = 0$. The numbers give the quantities of occupied valence bands (without Te(5s)).

FIG. 10. Intersections of the Fermi surface and Brillouin zone of ZrTe$_3$ with different k_y.

approximately parallel lines (small triangles) with almost pure Te(2)/Te(3)(5p_x) orbital character. These bands cause further E_F intersections along the lines $B = (-\frac{1}{2}, 0, 0) \rightarrow D = (-\frac{1}{2}, \frac{1}{2}, 0) \rightarrow Y = (0, \frac{1}{2}, 0)$ close to point D, where 18 p bands are occupied (the third branch is symbolized by rhombs). Large regions between these features show an occupation of 16 p bands, a number which corresponds together with the number of 6 Te(5s) bands to the total number of 44 valence electrons.

In the [001] direction the hole pocket region around points G evolves to bands of interconnected "double bubbles" with flattened spherical inclusions around points $Z = (0, 0, \frac{1}{2})$. This is shown in Fig. 10 by a sequence of Fermi surface cross sections with different k_y. Inside the spheres around points Z ($y = 0$ and $\frac{1}{48}$) again 16 bands are occupied. In the band structure (Fig. 4) this feature is found along the line G to Z, where one Zr(4d_{y^2}) band comes down in energy below E_F (see Fig. 8) and is raised again above E_F along the line Z to $C = (0, \frac{1}{2}, \frac{1}{2})$ (see Fig. 5a). Solely around point Z an occupation of Zr(4d_{y^2}) orbitals is found.

The undulating cross sections of the Te(2)/Te(3)(5p_x) orbital related Fermi surface between $y = 0$ and $y = \frac{1}{12}$ flatten out above $y = \frac{1}{4}$ to approximately parallel areas and reveal a nesting behavior. Since the parallelism of the Fermi surfaces for $y \geq \frac{1}{4}$ is not perfect, only a range of possible values for the nesting vector $\vec{q}$ can be given: from $y \approx \frac{1}{4}$ to $y = 0.5$, $\vec{q} \approx (0.95 \pm 0.05)\vec{a}* + (0.35 \pm 0.15)\vec{c}*$, connecting two electron pocket regions with occupation of 17 p bands (see Fig. 9). This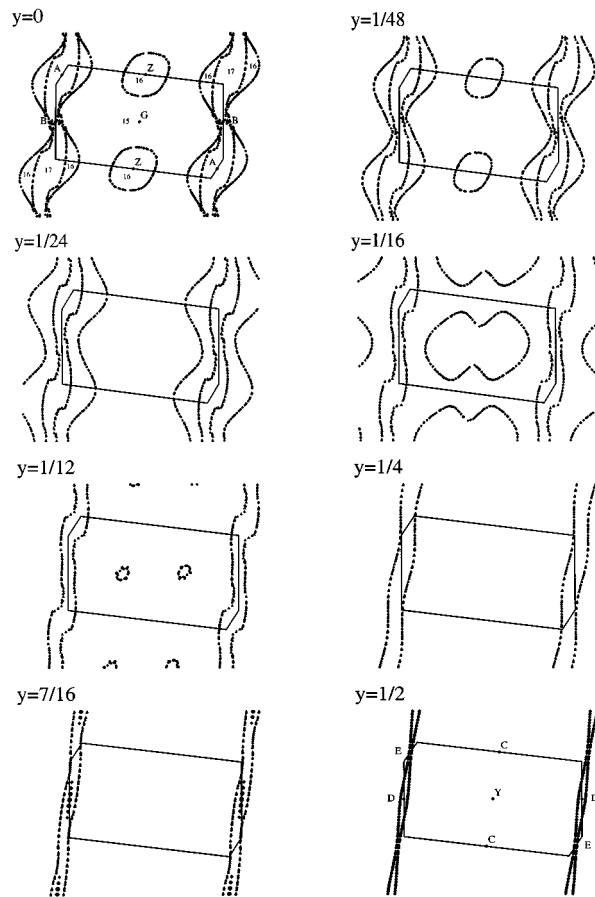 vector is in fair agreement with data from an electron diffraction study of ZrTe$_3$, which has shown the presence of a CDW with the vector $\vec{q} \approx 0.93\vec{a}* + 0.33\vec{c}*$ (19). Experimentally, holes are found to be associated with the resistivity hump at ~ 63 K (4).

DISCUSSION

Two formulas for metal trichalcogenides MQ_3 with linear Q^- chains are appropriate: (i) $M^{4+}Q^{2-}(Q_2)^{2-}$, implying dumbbells of singly bound Q^- ions as structural fragments and semiconducting behavior, or (ii) $M^{4+}Q^{2-}\frac{1}{\infty}[Q^-]_2$, implying chains of equidistant Q^- ions forming two equal bonds to the neighboring Q^- ions of bond order $\frac{1}{2}$ and metallic behavior.

Compounds featuring linear chalcogen chains of various formula types are summarized in Table 5. Exact equidistant chains are observed only in TlTe (20). In U$_2$Te$_5$ (21) two different types of linear Te chains are found: one type is nearly equidistant (concerning Te of the U(2) coordination polyhedron), a finding which is comparable to UTe$_2$ (22), and the second type shows a distinct alternation (Te around

TABLE 5
Summary of Compounds with Linear Chalcogen Chains as Structural Fragments[a]

Compound	d_1 (pm)	d_2 (pm)	d_2/d_1	Conductivity
ZrS$_3$[b]	208.8	303.6	1.45	sc
NbS$_3$[c]	205.0	291.4	1.42	sc
USe$_3$[d]	236.1	329.4	1.40	sc
ZrSe$_3$[b]	234.4	306.8	1.31	sc
UTe$_3$[e]	275.1	335.0	1.22	sc
ZrTe$_3$[f]	279.2	310.4	1.11	m
U$_2$Te$_5$: U(1)[g]	290.3	317.7	1.09	m
UTe$_2$(RT)[h]	305.7	307.6	1.01	m
U$_2$Te$_5$: U(2)[g]	303.3	304.7	1.00	m
TlTe[i]	308.5	308.5	1.00	m

[a] The distances given are calculated from single-crystal data (sc, semiconductor; m, metal).
[b] S. Furuseth, L. Brattås, and A. Kjekhus, *Acta Chem. Scand.*, *Sect. A* **29**, 623 (1975).
[c] J. Rijnsdorp and F. Jellinek, *J. Solid State Chem.* **25**, 325 (1978).
[d] A. Ben Salem, A. Meerschaut, and J. Rouxel, *C. R. Acad. Sci. Paris*, *Ser. II* **299**, 617 (1984).
[e] K. Stöwe, *Z. Anorg. Allg. Chem.* **622**, 1419 (1996).
[f] S. Furuseth and H. Fjellvåg, *Acta Chem. Scand.* **45**, 694 (1991).
[g] K. Stöwe, *Z. Anorg. Allg. Chem.* **622**, 1423 (1996).
[h] K. Stöwe, *J. Solid State Chem.* **127**, 202 (1996).
[i] A. A. Toure, G. Kra, R. Eholie, J. Oliver-Fourcade, and J.-C. Jumas, *J. Solid State Chem.* **87**, 229 (1990).

U(1)). Both uranium tellurides have metallic properties. Compounds with even larger alternations are found at the top of Table 5, with the alternation defined as d_2/d_1 ($d_1 < d_2$). For example, ZrS$_3$ and ZrSe$_3$ are semiconductors, because with 44 valence electrons per unit cell ($Z = 2$), the Fermi energy lies between the Q–Q $pp\sigma$-bonding and $pp\sigma$*-antibonding crystal orbitals. ZrTe$_3$ is found at the borderline separating semiconducting from metallic compounds. Despite distinct chain alternation, ZrTe$_3$ has metallic properties. The band occupation in the two closely related compounds UTe$_3$ and ZrTe$_3$ is shown schematically in Fig. 11 in the middle part and at the right side, respectively. Both compounds have very similar intrachain distance d_1, but d_2 is ≈ 25 pm smaller in ZrTe$_3$ than in UTe$_3$ ($d_{2'}$). Thus the bands are more dispersive in ZrTe$_3$ than in UTe$_3$, resulting in a smaller gap between $pp\sigma$ and $pp\sigma$* bands. Because of additional homonuclear Te distances below the sum of the radii of Te^{2-} ions in ZrTe$_3$ compared to UTe$_3$, dispersions of Te($5p$) bands other than of Te(2)/Te(3)($5p_x$) character are furthermore observed. The destabilization of one of the Te(1)($5p_y$) bands raises this band in ZrTe$_3$ above the bottom of the $pp\sigma$* states, leading to a depletion of the former one in favor of $pp\sigma$*-antibonding crystal orbitals. Therefore the dimensionality of the conductivity in ZrTe$_3$ is beyond that of the one-dimensional chain and the notation of the compound ZrTe$_3$ with Te(1)$^{2-}$ ions is not precise.
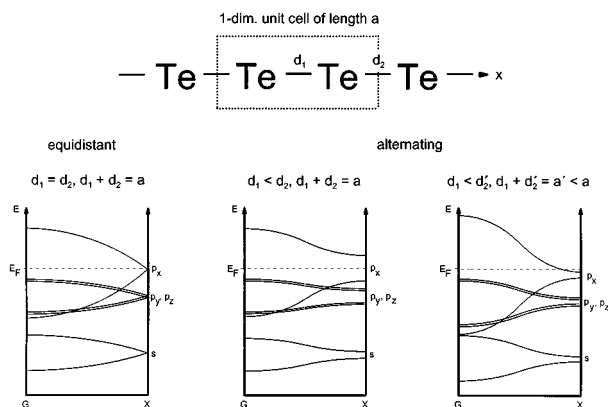

FIG. 11. Schematic dispersion relation of the bands of a linear one-dimensional Te chain: left, for an equidistant chain; middle, for an alternating chain with the same unit cell length a. On the right side the dispersion relation is shown for a smaller chain length a' at constant d_1. The Fermi energy was chosen to reflect the band occupation in UTe$_3$ (middle) and ZrTe$_3$ (right).

REFERENCES

1. S. Furuseth, L. Brattås, and A. Kjekhus, *Acta Chem. Scand.*, *Ser. A* **29**, 623 (1975).
2. S. Takahashi, T. Sambongi, and S. Okada, *J. Phys.*, *Colloq.* **C3**, 1733 (1983).
3. H. Nakajima, K. Nomura, and T. Sambongi, *Physica B* **143**, 240 (1986).
4. S. Takahashi, T. Sambongi, J. W. Brill, and W. Roark, *Solid State Commun.* **49**, 1031 (1984).
5. E. Canadell, Y. Mathey, and M.-H. Whangbo, *J. Am. Chem. Soc.* **110**, 194 (1988).
6. J. A. Wilson, *Philos. Trans. R. Soc. London*, *Ser. A* **314**, 159 (1985).
7. J. L. Hodeau, M. Marezio, C. Roucau, R. Ayroles, A. Meerschaut, J. Rouxel, and P. Monceau, *J. Phys. C: Solid State Phys.* **11**, 4117 (1978).
8. S. Furuseth and H. Fjellvåg, *Acta Chem. Scand.* **45**, 694 (1991).
9. SHELXTL PLUS, Version 4.0, Program for Determination of Crystal Structures with X-Ray and Neutron Data, Siemens Analytical X-Ray Instruments, Inc., Madison, WI, 1990.
10. G. Llabres and O. Dideberg, *Acta Crystallogr.*, *Sect. B* **28**, 2438 (1972).
11. K. Stöwe, *Z. Anorg. Allg. Chem.* **622**, 1419 (1996).
12. G. Krier, O. Jepsen, A. Burkhardt, and O. K. Andersen, Tight Binding LMTO-ASA Program, Version 4.7, Stuttgart, Germany.
13. O. Jepsen and O. K. Andersen, *Z. Phys. B* **97**, 35 (1995).
14. S. C. Miller and W. F. Love, "Tables of Irreducible Representations of Space Groups and Co-Representation of Magnetic Space Groups." Pruett Press, Boulder, CO, 1967.
15. E. Zintl and W. Dullenkopf, *Z. Phys. Chem. B* **16**, 195 (1932); E. Zintl and W. Hauke, *Z. Elektrochem.* **44**, 104 (1938); W. Klemm and E. Busmann, *Z. Anorg. Allg. Chem.* **319**, 297 (1963); H. Schäfer, B. Eisenmann, and W. Müller, *Angew. Chem.* **85**, 742 (1973); *Angew. Chem.*, *Int. Ed. Engl.* **12**, 694 (1973); W. B. Pearson, *Acta Crystallogr.* **17**, 1 (1964); H. G. von Schnering, *Angew. Chem.* **93**, 44 (1981); *Angew. Chem.*, *Int. Ed. Engl.* **20**, 33 (1981).

16. E.g.: H. Kuzmany, *in* "Festkörperspektroskopie," p. 107. Springer-Verlag, Berlin, 1990.

17. P. Horsch and H. Rietschel, *Z. Phys. B* **27,** 153 (1977); J. E. Hirsch and D. J. Scalapino, *Phys. Rev. Lett.* **56,** 2732 (1986); J. Labbe and J. Bok, *Europhys. Lett.* **3,** 1225 (1987); P. A. Lee and N. Read, *Phys. Rev. Lett.* **58,** 2691 (1987); J. Friedel, *J. Phys. Condens. Matter* **1,** 7757 (1989); R. S. Markiewicz, *Int. J. Mod. Phys. B* **5,** 2037 (1991).

18. J. Rijnsdorp and F. Jellinek, *J. Solid State Chem.* **25,** 325 (1978).

19. D. J. Eaglesham, J. W. Steeds, and J. A. Wilson, *J. Phys. C* **17,** L697 (1984).

20. A. A. Toure, G. Kra, R. Eholie, J. Olivier-Fourcade, and J.-C. Jumas, *J. Solid State Chem.* **87,** 229 (1990).

21. K. Stöwe, *Z. Anorg. Allg. Chem.* **622,** 1423 (1996).

22. K. Stöwe, *J. Solid State Chem.* **127,** 202 (1996).